13

Monitoring of Rocks and Underground Structures Using PZT and FBG Sensors

S. Bhalla*, Y. W. Yang, C. K. Soh
*Department of Civil Engineering, Indian Institute of Technology Delhi,
Hauz Khas, New Delhi 110016, India
Tel: 91-11-2659-1040; Fax: 91-11-2658-1117
Email: sbhalla@civil.iitd.ac.in

13.1 Introduction

This chapter discusses the feasibility of employing the new generation fiber optic and piezoelectric sensor systems for comprehensive monitoring of rocks, covering load history monitoring/retrieval as well as damage assessment. In several major cities across the world, city planners are paying serious attention to the development of usable underground space in the form of caverns and tunnels due to continuously depleting land availability (Zhao *et al*., 1999). In addition, underground structures are considered safer compared to surface structures against earthquakes and hurricanes, and are less prone to noise pollution (Goel, 2001). However, they demand huge resources for construction and maintenance, and any collapse could be detrimental to the nation's economy in terms of lives and properties. This necessitates their comprehensive monitoring on a regular basis to check the onset of damages. Damages might occur due to environment-induced degradation, fatigue, excessive/unpredicted loads, and underground blasts. In addition, instrumentation and monitoring of the underground structures during construction and operation can facilitate validation of key design assumptions. This is especially pertinent to the underground structures, since quite often, many geotechnical and environmental complexities cannot be accurately considered at the design stage. Comprehensive instrumentation can pave the way for long-term monitoring of external loads, stress distributions and deflections, which can be

C.-K. Soh et al. (eds.), *Smart Materials in Structural Health Monitoring, Control and Biomechanics*

useful for comparing the predicted and the actual responses as well as detecting the occurrence of structural damage in real-time, thereby ensuring a high level of safety. In addition, the database generated could economize future constructions.

In general, structural monitoring should cater for two requirements in the underground structures: (i) monitoring external loads (due to construction, vehicle movement, blasts, shocks and environmental effects) and corresponding deflections/strains, which can be termed as load history retrieval (LHR); and (ii) monitoring the occurrence of damages, that is, SHM. This chapter illustrates, using rock specimens, how PZT transducers can be utilized for SHM and FBG-based sensors for LHR simultaneously.

13.2 Conventional Versus Smart Material Based Sensor Systems for LHR and SHM of Underground Structures

Strain gauges are the most widely used sensors for LHR. The conventional strain gauges are based on vibrating wire or electrical resistance principle. Vibrating wire strain gauges (VWSGs) involve measuring the frequency of vibration of a pre-tensioned wire (whose ends are fixed to the monitored component) from which strain in the component is deduced. They are considered reliable for long-term strain monitoring, as demonstrated by Bakker (2000) on tunnels and Moyo (2002) on bridges. However, they are suitable for measuring static strains only, and are highly susceptible to mechanical noise from ambient vibrations. In addition, they are bulky and expensive. The electrical strain gauges (ESGs), which are based on stress dependence of a conductor's resistance, offer a low-cost alternative to VWSGs. On the other hand, the ESGs tend to be unstable over long periods of time due to decay, and hence are suitable for short-term monitoring only. Furthermore, they can be easily deteriorated by water and hence can be problematic if employed for monitoring underground rock structures such as caverns where damp conditions commonly occur. In general, both VWSGs and ESGs warrant separate cables from each sensing unit, which implies many wires for handling. At the same time, for long distance monitoring, these cables suffer from electro-magnetic interference and electrical noise, which further contaminates the measured strains.

In addition to strain gauges, extensometers are commonly employed for measuring displacements in underground structures, especially in newly constructed rock caverns. Generally, two types of extensometers are employed-tape extensometers and multiple point borehole extensometers. A tape extensometer consists of a telescopic rod, an invar bar, and a tape under constant tension placed between two measuring points, such as on the surface of a rock cavern. Hence, it measures relative displacements (convergence/divergence) between the two points. Multiple point borehole extensometers work on similar principle but can measure relative displacements between several points, such as

at various depths along a borehole. Both types of extensometers have been extensively employed for monitoring large caverns in Singapore (Zhao *et al*., 2002). However, the main limitation of the conventional extensometers is that they entail manual recording of data, which can be tedious. In tape extensometers, slight loosening of the convergence pins can severely affect the accuracy of the measurement since the displacements to be measured are in the range of a few millimeters. In addition, they tend to obstruct the usable area of the cavern. A more detailed review of sensors available for SHM can be found in Bhalla *et al*. (2005).

As far as SHM is concerned, several local and global techniques are currently under practice or are being investigated in several parts of the world, as explained in Part 1 of this book. However, these have so far not been applied on any underground structures. Similarly, not much research has been devoted to applying these materials to LHR and SHM of rocks. Following sections describe our study on the application of smart optical fiber and smart piezo-electric ceramic materials on LHR and SHM of rocks, respectively.

13.3 Experimental Investigations on Rocks

The experimental tests were performed by Yang *et al*. (2007) on three cylindrical specimens, each 50 mm in diameter and 100 mm in length, cored out from the Bukit Timah granite site in Singapore. Fig. 13.1 shows the instrumentation details of these specimens. Specimens 1 and 2 were instrumented with two ESGs (of a gauge length of 60 or 3 mm), two multiplexed FBG sensors (one for sensing strain and the other for temperature) and one PZT patch. Specimen 3 was instrumented with a PZT patch only. The ESGs were manufactured by Tokyo Sokki Kenkyujo Co, Ltd. (TML, 2004). They were bonded to the rock surface using quick set RS 850-940 epoxy adhesive (RS Components, 2004).

The two FBG-based strain gauges, manufactured by the Institute of Infocomm Research (I^2R) Singapore, had a length of 50 mm each. One of them was employed to record surface strain and the other for temperature compensation. The strain sensing FBG and the temperature sensing FBG were multiplexed. Temperature compensation is essential because FBG has relatively high sensitivity to temperature, measuring about 13 pm/°C against 1 pm for a micro-strain. Accordingly, the strain measuring FBG sensor was physically bonded to the specimen surface whereas the temperature measuring sensor was kept mechanically free. High strength epoxy adhesive RS 159-3957 (RS Components, 2004) was used for bonding the strain measuring FBG sensor for specimen 1 and quick set epoxy adhesive RS 850-940 was utilized for specimen 2. The PZT patches bonded to the specimens were 10 mm×10 mm×0.3 mm in size, conformed to grade PIC 151 (PI Ceramic, 2004), and were bonded to the rock specimens using the quick set epoxy adhesive RS 850-940.

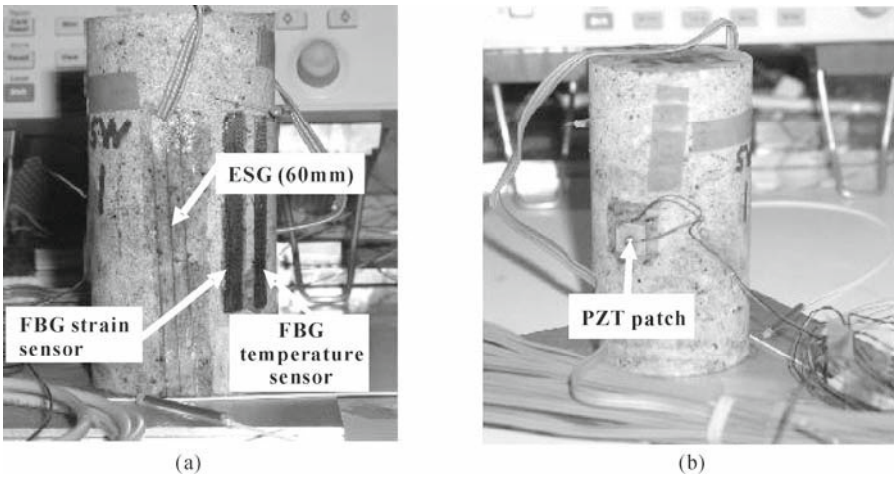

Fig. 13.1 Typical installation details of ESGs, FBG sensors and PZT patches on rock specimens. (a) ESG and FBG sensors; (b) PZT transducer

Fig. 13.2 shows the experimental setup for loading the test specimens and for measuring the responses of the ESG sensors and the PZT transducers. The PZT patch instrumented on the rock specimen was wired to a HP 4192A impedance analyzer (Hewlett Packard, 1996), which was controlled by a personal computer. The ESG sensors were wired to a strain recording data logger. The FBG sensors were wired to a micron-optics interrogator that was controlled by a notebook computer, as shown in Fig. 13.3.

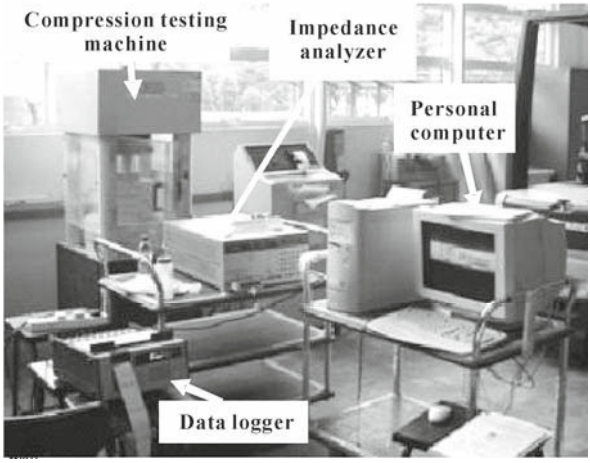

Fig. 13.2 Experimental setup showing compression testing machine, data logger (for ESGs) and impedance analyzer (for PZT transducers)

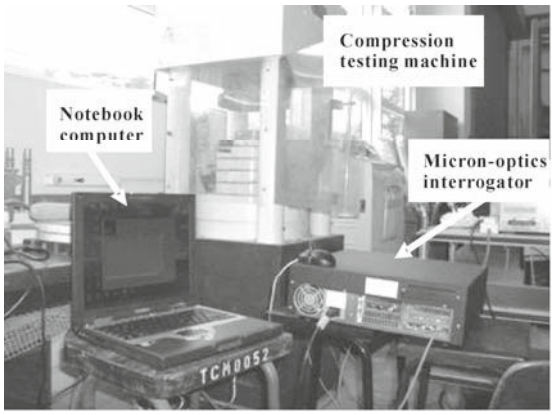

Fig. 13.3 Experimental setup showing compression testing machine and micron-optics interrogator (for interrogating FBG sensor)

Each rock specimen was compressed at a rate of 330 kN/min until the first predetermined load. It was then unloaded to zero load level at the same rate. Readings from the ESGs and FBGs were both recorded during loading and unloading at fixed intervals. After complete unloading, the conductance and susceptance signatures (real and imaginary components of admittance $\overline{Y}$) were acquired from the bonded PZT patch. In the next cycle, the specimen was compressed to the next higher level of load and the signatures of the PZT patch were acquired after unloading, as in the first cycle. This loading, unloading and signature acquisition process was repeated until failure. Thus, damage was induced to the rock specimens in a cyclic fashion.

13.4 LHR by ESG and FBG Sensors

13.4.1 Specimen 1

Fig. 13.4 shows the stress-strain history of specimen 1 obtained using the 3-mm ESG, the 60-mm ESG and the FBG-based strain sensors. From this figure, it is evident that the strain history retrieved by the 60-mm ESG (Fig. 13.4(b)) is similar to that by the FBG strain sensor (Fig. 13.4c). However, the strain measured by the 3-mm ESG is quite different from the other two strain gauges. This is because the 3-mm strain gauge tends to measure the local surface strain due to its small gauge length. The 60-mm ESG and 50-mm long FBG strain sensors, on the other hand, measure the overall surface strain and hence exhibit similar stress-strain plots. Fig. 13.5 compares the recordings from the 60-mm ESG and 50-mm FBG strain gauge for each load cycle. The load histories match quite well for cycles III, IV and V.

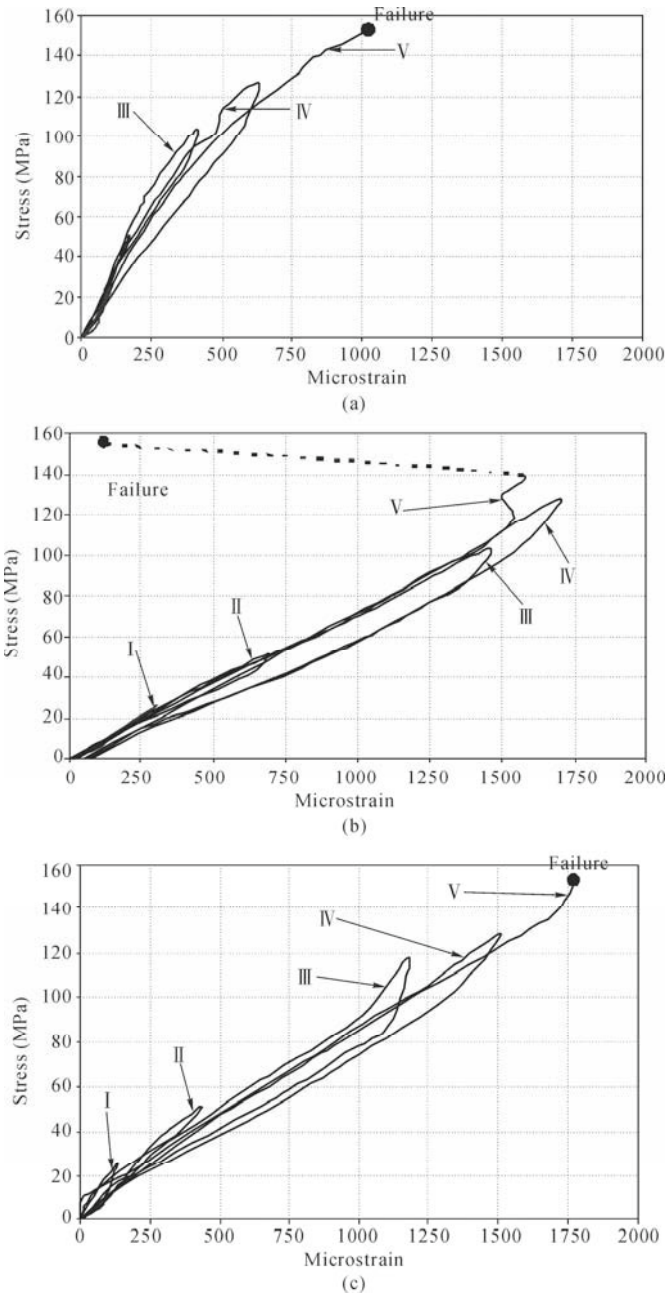

Fig. 13.4 Stress-strain histories for specimen 1 obtained using: (a) 3-mm ESG, (b) 60-mm ESG; (c) FBG based strain gauge

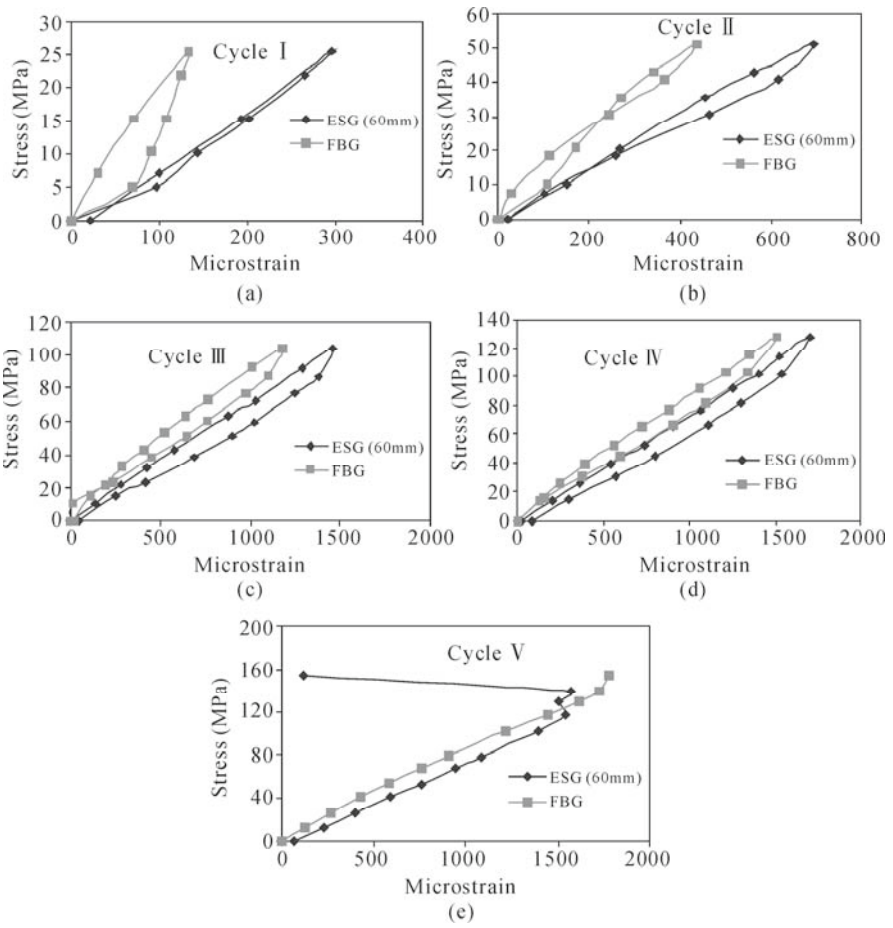

Fig. 13.5 Measurements of ESG (60 mm) and FBG (50 mm) sensor for each cycle for specimen 1. (a) Cycle I; (b) Cycle II; (c) Cycle III; (d) Cycle IV; (e) Cycle V

13.4.2 Specimen 2

Fig. 13.6 shows the stress-strain histories for specimen 2 obtained from the 3-mm ESG, the 60-mm ESG and the FBG-based strain sensors. Again, as in the case of specimen 1, strain history retrieved by the 60-mm ESG (Fig. 13.6(b)) is similar to that for the FBG strain sensor (Fig. 13.6(c)) but quite different from that for the 3-mm ESG (Fig. 13.6(a)). Fig. 13.7 compares the recordings of the 60-mm ESG and 50-mm FBG strain gauge for each load cycle. The load histories match very well for cycles IV, V and VI. Incidentally, both the 60-mm ESG and the FBG-based strain sensors failed prematurely during Cycle VI, well before failure of the specimen, which occurred during Cycle VIII.

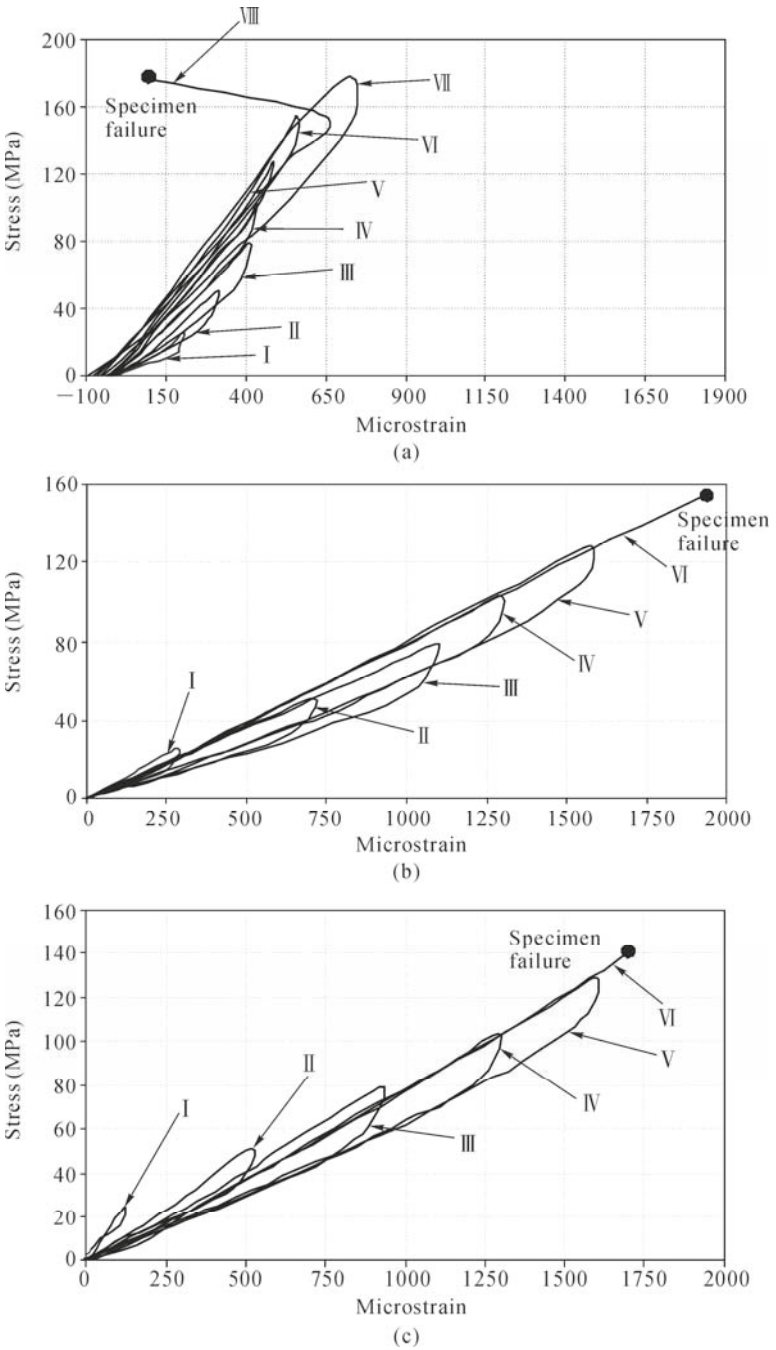

Fig. 13.6 Stress-strain histories for specimen 2 obtained using (a) 3-mm ESG; (b) 60-mm ESG; (c) FBG based strain gauge

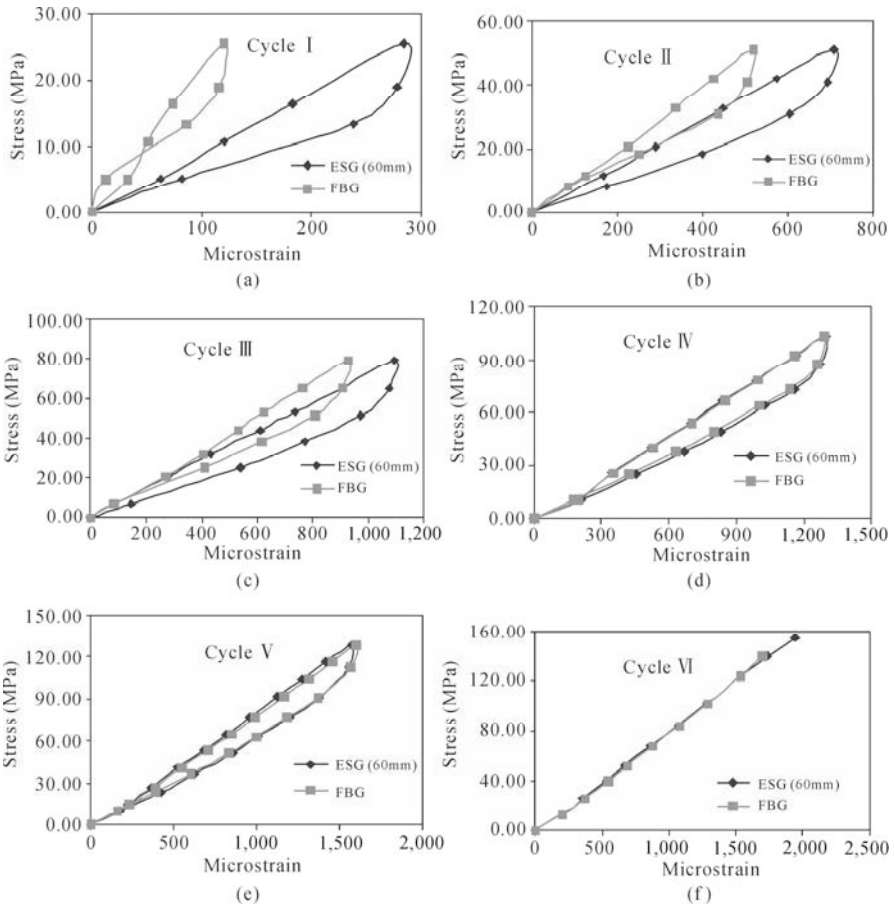

Fig. 13.7 Measurements of ESG (60 mm) and FBG (50 mm) sensor for each cycle for specimen 2. (a) Cycle I; (b) Cycle II; (c) Cycle III; (d) Cycle IV; (e) Cycle V; (f) Cycle VI

13.5 SHM by PZT Transducers

13.5.1 Specimen 1

Fig. 13.8 shows the conductance signatures acquired by the PZT patch bonded to specimen 1 at various stages during the loading process (in unloaded condition, after loading it to a specific load and then unloading). The signatures were acquired in a frequency range of 60 – 100 kHz at an interval of 100 Hz. In this figure, "load ratio" refers to the stress imposed on the specimen divided by the

ultimate stress (recorded at failure of the specimen). As shown in Fig. 13.4, the specimen was subjected to five load cycles and it failed during Cycle V, after withstanding a maximum stress of 154.3 MPa (corresponding to a load ratio = 1.0). During the loading process, when loaded up to load ratios of 0.33 and 0.66, the conductance plot underwent upward shifts. At the same time, major peaks shifted to the left, as shown in Fig. 13.9 for a frequency range of 90 – 100 kHz for load ratios of 0.0 and 0.33.

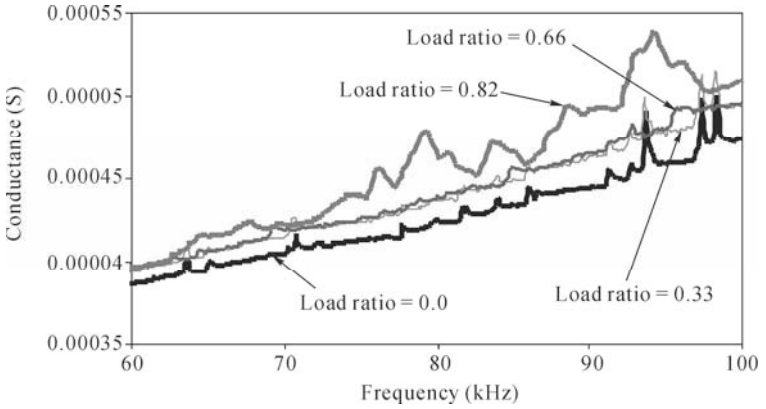

Fig. 13.8 Conductance signatures of PZT patch bonded to specimen 1 at various loading stages

Although the damage was incipient at a load ratio of 0.33, the conductance peaks underwent noticeable leftward shifts. Since the peaks represent structural resonance, leftward shifting of the peaks indicates loss of structural stiffness. Although visually no detectable damage was observed until a load ratio of 0.66, clear indication was however provided by the piezo-impedance signatures at a load ratio of 0.33. Furthermore, as apparent from Fig. 13.8, at a load ratio of 0.82, there is a very significant shift in the conductance signature indicating the occurrence of severe damage in the specimen. Careful examination of the specimen revealed the presence of a vertical crack running longitudinally across the specimen. Thus, by carefully observing the raw conductance signatures, it is possible to qualitatively infer the nature and magnitude of damage occurring in the host structure. Rigorous calibration for quantitative prediction is carried out in the next section. The PZT patch was found broken at the failure load, so conductance signature could not be recorded at a load ratio of 1.0.

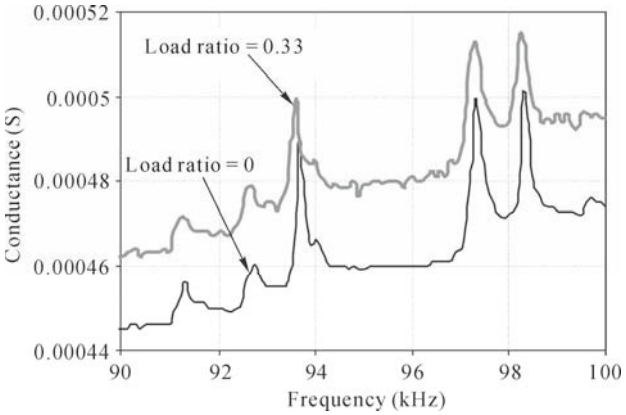

Fig. 13.9 Shifting of peaks of conductance signatures for PZT patch on specimen 1

13.5.2 Specimen 2

Fig. 13.10 shows the conductance signatures of the PZT patch bonded to specimen 2. As clearly observed from the figure, the conductance signature underwent consistent drifts with increasing load ratios. Fig. 13.11 shows the shifts in the peaks with damage progression in the frequency range of 92 – 93 kHz. These figures demonstrate that it is possible to detect both incipient and severe damages using PZT transducers. The PZT patch was able to sustain high strains of up to 2,000 micro-strain and was functioning well even after failure of the specimen.

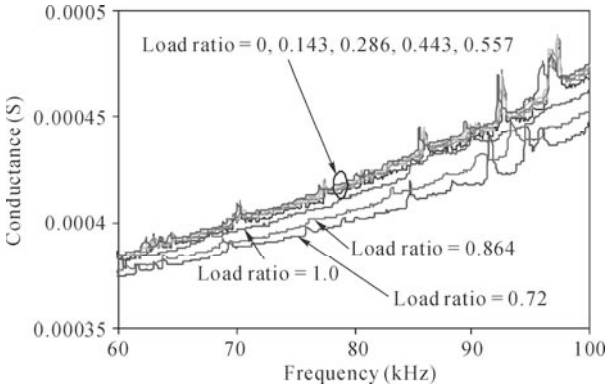

Fig. 13.10 Conductance signatures of PZT patch bonded to specimen 2 at various loading stages

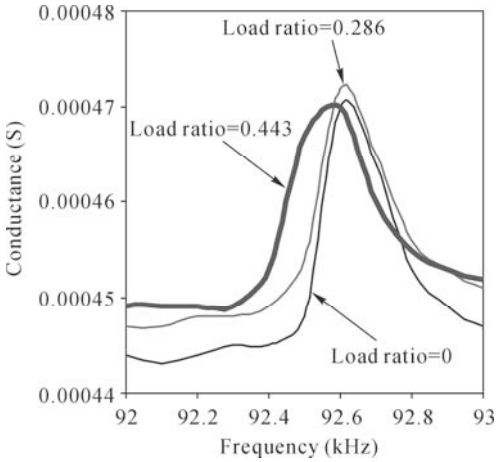

Fig. 13.11 Shifting of peaks of conductance signatures for PZT patch on specimen 2

13.5.3 Specimen 3

Fig. 13.12 shows the conductance signatures acquired by the PZT patch bonded to specimen 3 at various loading stages. Leftward shift of the resonance peaks (and hence indication of stiffness loss) is clearly evident from the figure. Similar to specimens 1 and 2, the results of specimen 3 also confirm the high sensitivity of the PZT transducers to the occurrence of damage. This specimen withstood a stress of 101.9 MPa (load ratio = 1.0) during Cycle VI. During Cycle VII, it failed at a stress of 50.9 MPa (corresponding signature marked as "after failure" in Fig. 3.12).

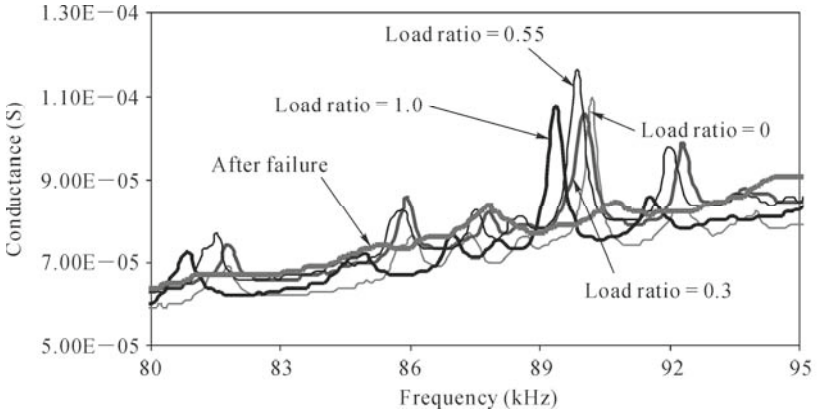

Fig. 13.12 Conductance signatures of PZT patch bonded to specimen 3 at various loading stages

13.5.4 Extraction of Structural Mechanical Impedance

Although it is possible to detect and qualitatively predict the level of damage from raw conductance signatures, as shown in Chapter 4, the real and imaginary components of the admittance signature can together be utilized to identify the host structural system as well as quantify damage more realistically. The first step is to extract the host structure's mechanical impedance from the admittance signatures, as outlined in Chapter 4. A close look at the variations of "x" and "y" (real and imaginary components of the extracted mechanical impedance) indicates a system behavior similar to a series combination of spring, damper and mass (system 7 of Table 4.1), for which the following relations hold true (Hixon, 1988)

$$x = \frac{c^{-1}}{c^{-2} + (\omega/k - 1/(\omega m))^2} \quad \text{and} \quad y = \frac{-(\omega/k - 1/(\omega m))}{c^{-2} + (\omega/k - 1/(\omega m))^2} \tag{13.1}$$

In addition, at frequency $\omega = \omega_o$, at which $y = 0$

$$k = m\omega_o^2 \tag{13.2}$$

Solving Eqs. (13.1) and (13.2) simultaneously, the system parameters k, c and m are derived at any frequency as

$$c = \frac{x^2 + y^2}{x} \tag{13.3}$$

$$m = \frac{cy(\omega^2 - \omega_o^2)}{(x - c)\omega\omega_o^2} \tag{13.4}$$

and

$$k = \frac{cy(\omega^2 - \omega_o^2)}{x(x - c)\omega} \tag{13.5}$$

Using these equations, the system parameters are derived at each measurement point within the frequency range and the average values then obtained. For specimen 1, the average parameters were found to be: c = 46.8813 N·s/m, k = 2.8776×10^7 N/m and m = 1.7851×10^{-4} kg. Fig. 13.13 compares the experimental plots of x and y with those of the equivalent system based on the computed average values of the parameters k, c and m. Reasonable agreement can be observed from the figure. The parameters were similarly worked out at various load ratios for specimen 1 as well as specimen 2.

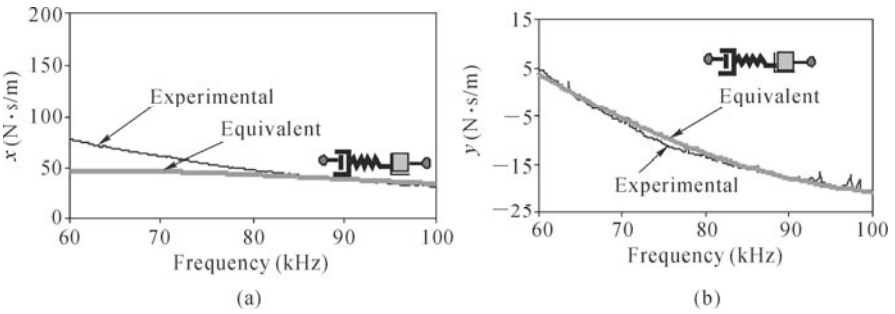

Fig. 13.13 Comparison between experimental and equivalent system impedance plots for specimen 1. (a) x vs. frequency; (b) y vs. frequency

13.5.5 Calibration of Extracted Parameters for Damage Quantification

Chapter 5 establishes an impedance-based damage model for concrete based on the identified stiffness parameter k. In the frequency range 60 – 100 kHz, concrete essentially behaves as a parallel spring-damper combination. On the other hand, in the case of rock specimens, the PZT patches identified the structure as a series combination of m, k and c (Fig. 13.13). A similar trend with respect to k is observed for the rock specimens. The identified stiffness is found to gradually reduce with damage. This is evident from the plots of k shown in Fig. 13.14, corresponding to different load ratios, for specimens 1 and 2. For specimen 1, there is slight increase at small load ratios but at higher load ratio, there is an overall reduction. For specimen 2, on the other hand, a very consistent reduction is observed.

At j^{th} frequency, a damage variable, D_j, can be defined in terms of the identified stiffness, similar to the case of concrete (Chapter 5), as

$$D_j = 1 - \frac{k_{dj}}{k_{oj}} \quad (0 < D_j < 1) \tag{13.6}$$

where k_{oj} is the equivalent spring stiffness at the j^{th} measurement point in the pristine state, and k_{dj} represents the corresponding value after damage. From the theory of continuum damage mechanics, an element can be deemed to fail if $D > D_c$. However, it is not possible to define a unique value of D_c due to unavoidable uncertainties related to rock and PZT patches. The damage variable is computed at each frequency in the interval 80 – 100 kHz, corresponding to each load ratio for specimens 1 and 2. Statistical examination of the data indicates that the damage variable follows a normal probability distribution. This is evident in Fig. 13.15, which shows the empirical cumulative probability distribution of D and also the theoretical normal probability distribution for specimens 1 and 2 at or near failure.

The normal distribution is found to be acceptable under 85% confidence limit for both specimens.

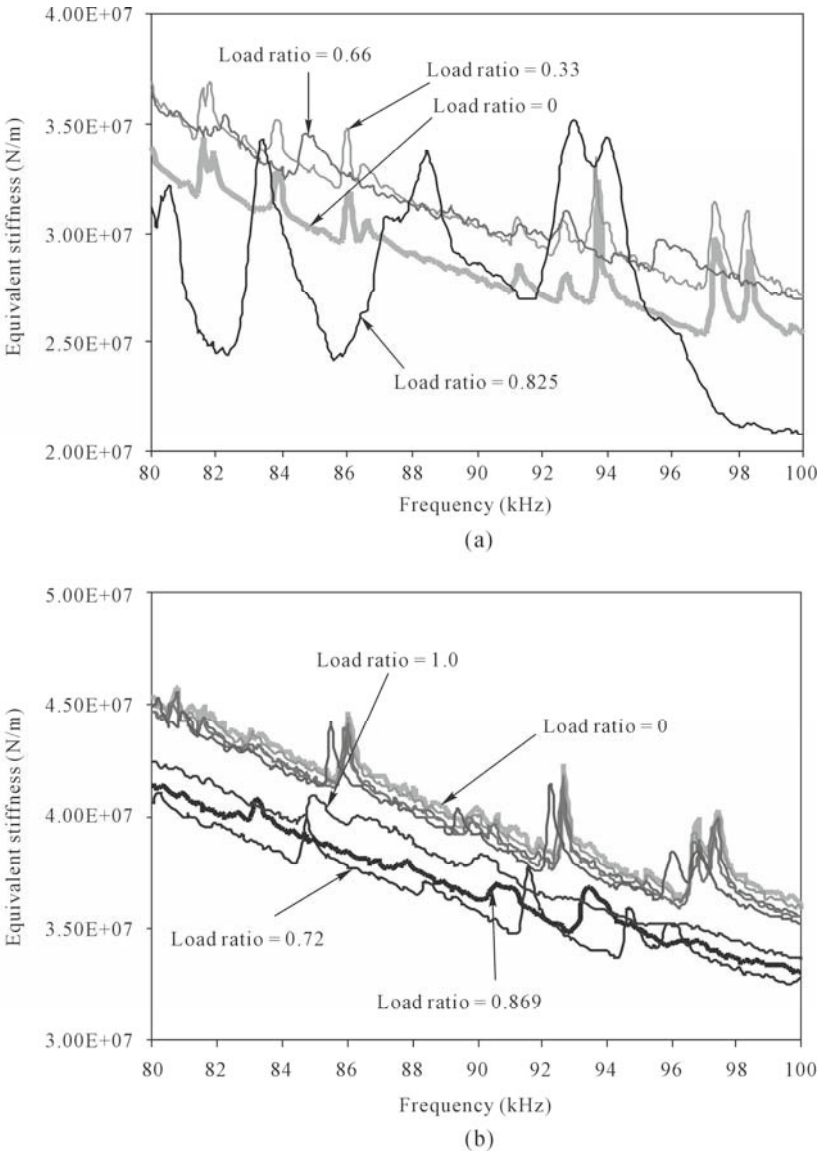

Fig. 13.14 Variation of identified spring stiffness with damage progression. (a) Specimen 1; (b) Specimen 2

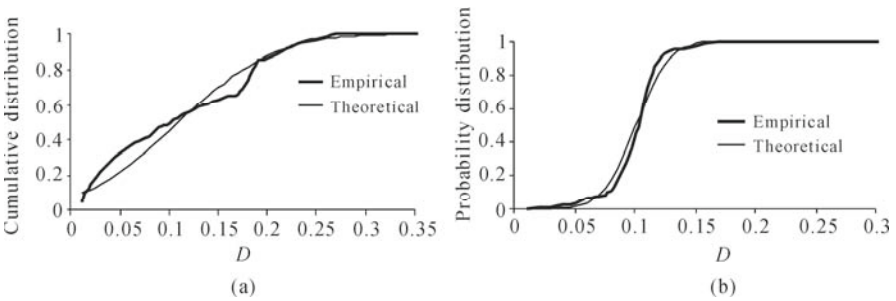

Fig. 13.15 Theoretical and empirical cumulative probability distributions near failure. (a) Specimen 1; (b) Specimen 2

Using the fuzzy set theory, a fuzzy region may be defined in the interval (D_L, D_U). $D > D_U$ represents a failure region with 100% failure possibility and $D < D_L$ represents a safe region with 0% failure possibility. Within the fuzzy or the transition region, that is, $D_L < D < D_U$, the failure possibility could vary between 0 and 100%. A characteristic or a membership function f_m can be defined ($0 < f_m(D) < 1$) to express the grade of failure possibility within the region (D_L, D_U). The fuzzy failure probability (FFP) can then be determined by Eq. (5.12) as in the case of concrete. Based on observations made during the tests, D_L and D_U were chosen as 0.0 and 0.12, respectively. Furthermore, the sinusoidal membership function given by Eq. (5.14) is adopted as in the case of concrete.

Using this membership function, the fuzzy failure probability (FFP) was worked out for the two specimens at each load ratio. At a load ratio of 0.7, which can be regarded as a state of severe damage, both specimens exhibited a fuzzy failure probability of greater than 70%. Fig. 13.16 shows the FFP of the specimens at various stages during the tests.

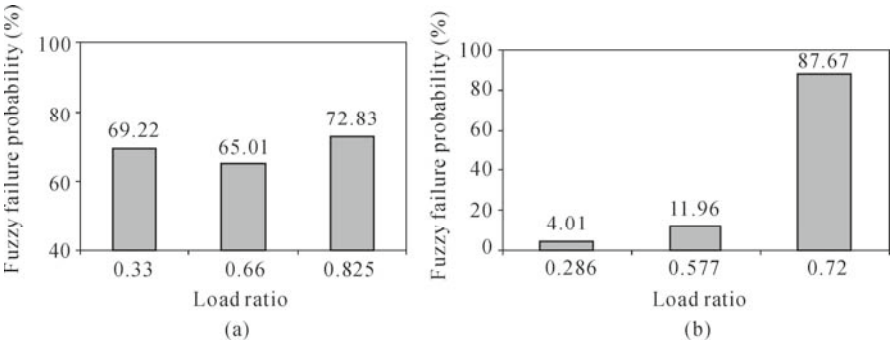

Fig. 13.16 Fuzzy failure probability of specimens 1 and 2 at various load ratios. (a) Specimen 1; (b) Specimen 2

Based on minute observations made during the tests on rock specimens, the following classification of damage is recommended based on FFP.

(1) FFP < 30% Incipient Damage (Micro-cracks);

(2) 30% < FFP < 50% Moderate damage (Cracks opening up);
(3) 50% < FFP < 70% Severe damage (large visible cracks);
(4) FFP > 70% Failure imminent.

Thus, the fuzzy probabilistic approach quantifies the extent of damage on a uniform 0 – 100% scale, which can be employed to evaluate damage in real-life rock structures, such as caverns and tunnels.

13.6 Robustness of PZT Transducers and FBG-based Strain Gauges

In our experimental study, three types of sensors were evaluated for their application on rocks, namely, PZT transducers, ESGs and FBG-based strain sensors. Fig. 13.17 shows close-up views of the three specimens after failure. The PZT patches were found to be intact and functioning well in specimens 2 and 3. However, the PZT patch bonded to specimen 1 broke at a load ratio of 0.826 because the failure crack passed directly through the location of the PZT patch, as shown in Fig. 13.17(a). In spite of this fracture, no debonding was observed between the PZT patch and the host rock surface. Hence, RS 840-950 epoxy adhesive is suitable for bonding PZT patches on rock surfaces. As observed from Figs. 13.17(c) and (e), the PZT patch was intact in both specimens 2 and 3.

The 60 mm long ESGs worked well until failure in specimen 1 (Fig. 13.17(a)), but failed prematurely at a load ratio of 0.868 in the case of specimen 2 (Fig. 13.17(d)). However, some debonding was noticed between the specimen and the sensor in the case of both specimens 1 and 2, as seen in Figs. 13.17(b) and 13.17(d).

The FBG sensors performed well at low loads in the case of specimen 1, but failed prematurely during Cycle VI (somewhere prior to failure of the ESG) in the case of specimen 2. As noticed from Figs. 13.17(b) and 13.17(d), significant debonding occurred between the rock surface and the FBG sensor prior to specimen failure. Hence, future tests need to be conducted to find a more robust adhesive for these sensors.

13.7 Potential Applications of Smart Sensors on Rock Structures

This chapter has demonstrated the feasibility of employing smart piezo-impedance transducers for SHM and FBG-based strain sensors for LHR of rock structures. PZT transducers show long-term durability and fast dynamic response, have low cost, exhibit negligible aging, and are immune to ambient noise. They facilitate direct estimation of damage without warranting analytical/numerical modeling. They can be used for wide ranging applications on rock structures such as assessing the condition of rocks after underground blasts, detection of cracks in caverns during the convergence period, monitoring the condition of rock bolts,

rock quality/strength assessment and measurement of dynamic strains. The results confirm that they are reliable damage indicators, and can warn of any imminent damage before it could be physically visible. The fuzzy probabilistic damage model quantifies damage realistically, and could be employed for damage diagnosis of real-life rock structures such as caverns and tunnels.

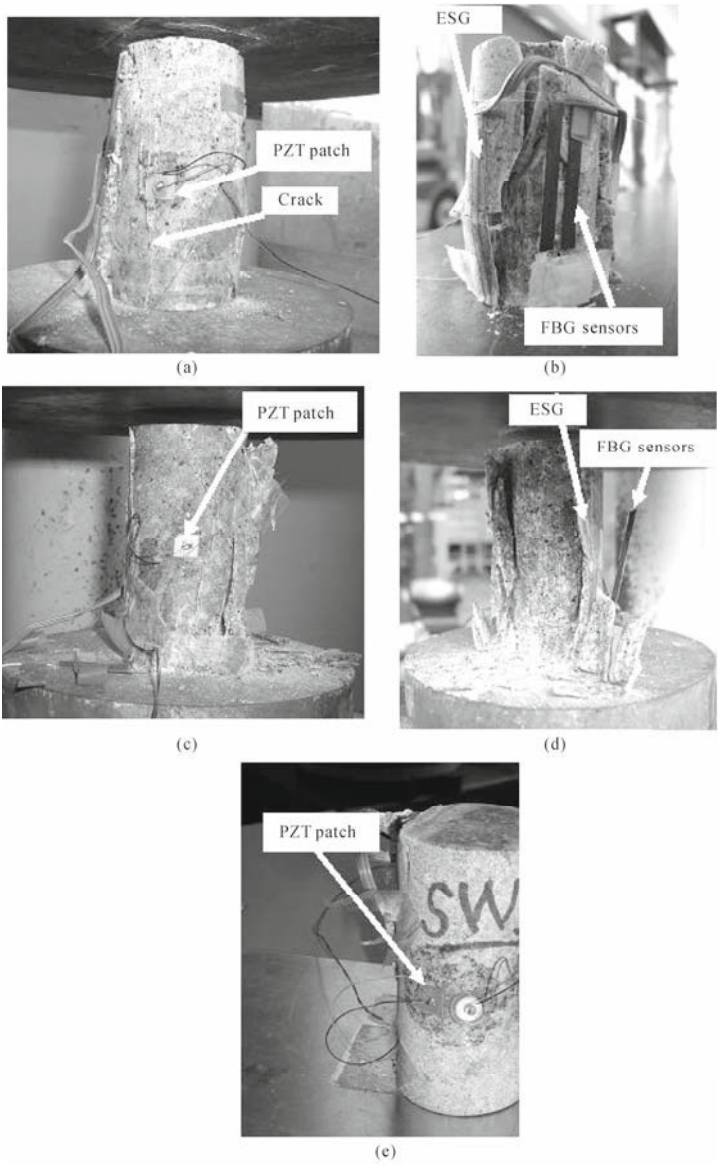

Fig. 13.17 Condition of specimens after failure. (a) Specimen 1: PZT patch; (b) Specimen 1: FBG and ESG; (c) Specimen 2: PZT patch; (d) Specimen 2: FBG and ESG; (e) Specimen 3: PZT patch

FBG sensors are characterized by long-term stability, are chemically inert and small sized, and carry the potential of eliminating cables that are troublesome in data transmission and retrieval. In rock structures, in addition to monitoring the static and dynamic strains in tunnels, caverns and rock bolts, these could be employed for precise measurement of cavern deflections/convergence, and long-term soil/rock movements. Thus, as PZT patches can perform SHM well and FBG sensors can facilitate LHR, they complement each other in structural monitoring.

References

Bakker, K. J. (2000). "Soil retaining structures: development of models for structural analysis", *Ph.D. Thesis*, Delfts University of Technology, Netherlands.

Bhalla, S., Yang, Y.W., Zhao, J. and Soh, C.K. (2005). "Structural health monitoring of underground facilities—technological issues and challenges", *Tunnelling and Underground Space Technology*, 20: 487-500.

Goel, R.K. (2001). "Status of tunnelling and underground construction activities and technologies in India", *Tunnelling and Underground Space Technology*, 16:63-75.

Hixon, E.L. (1988). "Mechanical impedance", *Shock and Vibration Handbook*, edited by C. M. Harris, 3rd ed., Mc Graw Hill Book Co., New York.

Hewlett Packard (1996). *HP LF 4192A impedance analyzer*, Operation manual, Japan.

Moyo, P. (2002). "Structural performance monitoring and health assessment of highway bridges", *Ph.D. Thesis*, Nanyang Technological University, Singapore.

PI Ceramic (2004). *Product Information Catalogue*, Lindenstrabe, Germany, http://www.piceramic.de.

RS Components (2004). Northants, UK, http://www.rs-components.com.

TML (2004). *Tokyo Sokki Kenkyujo Co. Ltd.* , Tokyo.

Yang, Y.W., Bhalla, S., Wang, C., Soh, C.K. and Zhao, J. (2007). "Monitoring of rocks using smart sensors", *Tunnelling and Underground Space Technology*, 22: 206-221.

Zhao, J., Liu, Q., Lee, K.W., Choa, V. and Teh, C.I. (1999). "Underground cavern development in the Jurong sedimentary rock formation", *Tunnelling and Underground Space Technology*, 14: 449-459.

Zhao, J., Cai, J.G., Tunbridge, L., Song, H.W., Zhang, X.H. and Zhao, X.B. (2002). "Results of rock cavern monitoring and assessment of cavern stability", *Technical report for NTU-DSTA Joint R&D Project on instrumentation and monitoring of rock caverns during construction and operation*.